52nd AIAA/ASME/ASCE/AHS/ASC Structures, Structural Dynamics and Materials Conference
4 - 7 April 2011, Denver, Colorado

AIAA 2011-1770

Efficient Creation of Aeroservoelastic Models Using Interpolated Aerodynamics Models

Daniel C. Hammerand[*], James M. Gariffo[†], and Kevin M. Roughen[‡]
M4 Engineering, Inc. 4020 Long Beach Blvd., Long Beach, CA, 90807, USA

The expense of running computational fluid dynamics (CFD) and computational structural dynamics (CSD) codes motivates the creation of aeroservoelastic models which can be interpolated accurately to unmodeled flight conditions. Furthermore, both the analyzed and interpolated points can be used to design modern control laws for flutter suppression, gust load alleviation, and ride quality enhancement. One interpolation method involves taking the weighted average of the assembled aeroservoelastic models themselves. One shortcoming of such a methodology is the inability to create additional aeroservoelastic models that correspond to changing the dynamic pressure, since the aerodynamics and structural dynamics have been combined together. For linear representations, the aerodynamics are taken to change linearly with the dynamic pressure. Hence, it should be a straightforward task to create additional linear aeroservoelastic models that correspond to changing the dynamic pressure only. The present study examines just such a possibility in detail. A consistent basis is used for interpolating the aerodynamic models is used to produce accurate models that can be safely combined with the structural and actuator models in generating the final aeroservoelastic models. The results presented for the AGARD 445.6 wing demonstrate the efficiency of interpolating the aerodynamic model separately before integrating into the aeroservoelastic model. The effectiveness of creating a control law for flutter suppresion for such interpolated points is shown for a subsonic case.

I. Introduction

Major improvements in computational hardware, software, and methodologies over the past couple of decades have led to the development of sophisticated mathematical models to represent the aeroelastic response of flight vehicles.[1] With the addition of models for the active control of control surfaces, these aeroelastic models become aeroservoelastic models. While enabling the design of active control systems for flutter suppression, gust load alleviation, and ride quality enhancement, these aeroservoelastic models can quickly become prohibitively expensive to create during the initial stages of a preliminary design or the early stages of a design modification. Efficient creation of such models can be critical to the success of a development program.

The present work aims to address this through the creation of additional aeroservoelastic models using interpolation. In particular, the aerodynamic portion of the models will be interpolated prior to assembly into the integrated aeroservoelastic model. Since the aerodynamic portion of the aeroservoelastic model scales linearly with the dynamic pressure, it is a straightforward task to create a family of such interpolated aeroservoelastic models, each corresponding to the same flight condition, but with the dynamic pressure changed. This allows for a rather straightforward technique to determine the flutter characteristics away from points that have been analyzed directly.

The aerodynamics will be determined using generalized aerodynamic forces (GAFs) to represent the unsteady aerodynamic forces computed using the doublet-lattice method (DLM) or a finite volume computational fluid dynamics (CFD) code employing Euler equations. The accuracy of these type of CFD GAF models in the transonic regime is demonstrated and relies upon the simple principle of linearization about the proper nonlinear condition.

---

[*] Senior Engineer, Research, dhammerand@m4-engineering.com, AIAA senior member

[†] Engineer, Research, jgariffo@m4-engineering.com, AIAA student member

[‡] Vice President of Engineering, kevin.roughen@m4-engineering.com, AIAA member

Although not investigated here, the present study motivates the future work of interpolating the structural dynamics model before assembly into a complete aeroservoelastic model. Such an interpolation/averaging may correspond to accounting for different mass conditions such as fuel weight, cargo load, or passenger load conditions.

The next sections detail the development of the aeroservoelastic model which follows the methodology developed in Ref. 2. Essentially, the finite element method is used to compute the structural modal mass, stiffnesses, and damping matrices. The unsteady system aerodynamics is computed using either potential flow via the DLM[3,4] or the Euler equations via CFD.[5] State-space equations for the aerodynamics are developed using either Roger's Rational Function Approximation (RFA)[6] in the reduced frequency domain.

II. Structural Dynamics

The equations for the structural dynamics portion are

$$[M]\{\ddot{d}\} + [C]\{\dot{d}\} + [K]\{d\} = \{F_{aero}\} + \{F_{act}\} \tag{1}$$

where $[M]$, $[C]$, and $[K]$ are the mass, damping, and stiffness matrices determined using finite elements, $\{F_{aero}\}$ gives the aerodynamic forces, and $\{F_{act}\}$ gives the actuator forces. Here proportional damping will be used such that

$$[C] = \alpha_1[M] + \alpha_2[K] \tag{2}$$

This enables the relevant modal free vibration problem to be written by temporarily ignoring damping as follows:

$$[M]\{\ddot{d}\} + [K]\{d\} = \{0\} \tag{3}$$

The solution to Eq. (3) is simply

$$\{d\} = e^{i\omega t}\{\phi\} \tag{4}$$

which results in the following generalized eigenvalue problem:

$$[K]\{\phi\} = \omega^2[M]\{\phi\} \tag{5}$$

Here $\{\phi\}$ is the vector of modal displacements. The system of equations is reduced to modal form by employing

$$\{d\} = [\Phi]\{\xi(t)\} \tag{6}$$

in Eq. (1) to give

$$[\tilde{M}]\{\ddot{\xi}\} + [\tilde{C}]\{\dot{\xi}\} + [\tilde{K}]\{\xi\} = \{\tilde{F}_{aero}\} + \{\tilde{F}_{act}\} \tag{7}$$

where

$$\begin{aligned}
[\tilde{M}] &= [\Phi]^T[M][\Phi] && (8)\\
[\tilde{C}] &= [\Phi]^T[C][\Phi] && (9)\\
[\tilde{K}] &= [\Phi]^T[K][\Phi] && (10)\\
\{\tilde{F}_{aero}\} &= [\Phi]^T\{F_{aero}\} && (11)\\
\{\tilde{F}_{act}\} &= [\Phi]^T\{F_{act}\} && (12)
\end{aligned}$$

Although it is possible to rewrite Eq. (7) in state-space form at this point, it is prudent to first write expressions for the aerodynamic and actuator forces.

III. Aerodynamics Model

For a single flight condition, the aerodynamic model is generated using the DLM method or CFD. In each case, the goal is to develop discrete data for the generalized aerodynamic forces as a function of reduced frequency. Using DLM, such GAF data results directly. However, for the CFD based approach, data for the modal aerodynamic forces for a specified modal displacement is first determined in the time domain. This time domain data is given by $q_{ij}(t)$ where

$$q_{ij}(t) = \text{force in the i}^{\text{th}}\text{ mode for unit displacement in the n}^{\text{th}}\text{ mode and } q_\infty = 1 \tag{13}$$

The present CFD methodology is based upon exciting one mode at a time using a Gaussian pulse while holding the other modes fixed. The resulting discrete time domain data is transformed to the frequency domain using the discrete Fourier transform as follows:

$$Q_{ij}(\omega_m) = \frac{1}{q_\infty}\frac{DFT(\tilde{F}_{aero-i}(t_n))}{DFT(\xi_j(t_n))} = \frac{1}{q_\infty}\frac{\tilde{F}_{aero-i}(\omega_m)}{\Xi_j(\omega_m)} \tag{14}$$

where ω_m represents the m^{th} angular frequency. However, for Roger's RFA, the GAFs are needed in the reduced frequency domain where the reduced frequency k for a general angular frequency ω is given by

$$k = \frac{c}{2V_\infty}\omega \tag{15}$$

or

$$k = \frac{\omega}{a} = \frac{\omega}{2V_\infty/c} \tag{16}$$

where c represents the characteristic wing chord and V_∞ is the free stream velocity. Here, $a = 2V_\infty/c$ is the scale factor relating the frequency domain to the reduced frequency domain. Using the standard formula for stretching/shrinking the frequency domain which corresponds to shrinking/stretching the time domain, the GAFs as a function of reduced frequency are given by

$$\begin{aligned} Q_{ij}(k_m) &= \frac{1}{q_\infty}\frac{DFT(\tilde{F}_{aero-i}(at_n))}{DFT(\xi_j(at_n))} && (17)\\ &= \frac{1}{q_\infty}\frac{\tilde{F}_{aero-i}(\omega_m/a)}{\Xi_j(\omega_m/a)} && (18)\\ &= \frac{1}{q_\infty}\frac{\tilde{F}_{aero-i}(k_m)}{\Xi_j(k_m)} && (19)\end{aligned}$$

Once this data has been written in the reduced frequency domain for the complete set of GAFs, it is fit using Roger's Rational Function Approximation as follows:

$$[Q(p)] = [A^0] + p[A^1] + p^2[A^2] + \sum_{l=1}^{N_l}\frac{p\,[B^l]}{p+\beta^l} \tag{20}$$

where $p = ik$ with $i = \sqrt{-1}$. Here, the $[B^l]$ terms will lead the aerodynamic lag states in the time domain. The corresponding time domain state-space model is given as follows:

$$\{\dot{z}\} = [A_A]\{z\} + [B_A]\left\{\begin{array}{c}\xi\\ \dot{\xi}\\ \ddot{\xi}\end{array}\right\} \tag{21}$$

$$\{\tilde{F}_{aero}\} = q_\infty\left([C_A]\{z\} + [D_A]\left\{\begin{array}{c}\xi\\ \dot{\xi}\\ \ddot{\xi}\end{array}\right\}\right) \tag{22}$$

where q_∞ is the free stream dynamic pressure, $\{z\}$ is a vector of aerodynamic lag states and $\{\xi\}$ is the vector of modal displacements from before. This equation is written in expanded form as

$$\{\dot{z}\} = [A_A]\{z\} + [\begin{array}{ccc}0 & B_A^1 & 0\end{array}]\left\{\begin{array}{c}\xi\\ \dot{\xi}\\ \ddot{\xi}\end{array}\right\} \tag{23}$$

$$\{\tilde{F}_{aero}\} \quad = \quad q_\infty \left([C_A]\{z\} + \begin{bmatrix} D_A^0 & D_A^1 & D_A^2 \end{bmatrix} \left\{ \begin{array}{c} \xi \\ \dot{\xi} \\ \ddot{\xi} \end{array} \right\} \right) \tag{24}$$

Here the aerodynamic state-space matrices are determined from the terms in Eq. (20) as follows:

$$[A_A] \quad = \quad \frac{2V_\infty}{c} diag\left(-\beta^1, -\beta^2, \ldots, -\beta^{N_l}\right) \tag{25}$$

$$[B_A^1] \quad = \quad \begin{bmatrix} \hat{B}_A & 0 & 0 \\ 0 & \ddots & 0 \\ 0 & 0 & \hat{B}_A \end{bmatrix} \tag{26}$$

$$[C_A] \quad = \quad \begin{bmatrix} B^1 & B^2 & \ldots & B^{N_l} \end{bmatrix} \tag{27}$$

$$[D_A^0] \quad = \quad [A^0] \tag{28}$$

$$[D_A^1] \quad = \quad \frac{c}{2V_\infty}[A^1] \tag{29}$$

$$[D_A^2] \quad = \quad \left(\frac{c}{2V_\infty}\right)^2 [A^2] \tag{30}$$

with

$$\{\hat{B}_A\} = \left\{ \begin{array}{c} 1 \\ 1 \\ \vdots \\ 1 \end{array} \right\} \quad (N_l \times 1) \tag{31}$$

IV. Actuator Models

In addition to the modeling the structure and aerodynamics, a model is included in the aeroservoelastic state space model for the actuators that regulate the control surface. This is done by modeling the actuators as a feedback control system with gains $[k]$ and delay constants $[a]$. Here the nodal actuator forces can be written as

$$\{F_{act}\} = [k]\left(\{\delta_{cmd}\} - \{\delta\} - [a]\{\dot{\delta}\}\right) \tag{32}$$

For the control surface deflections, the modal expansion is given by

$$\{\delta\} = [r]\{\xi\} \tag{33}$$

where $[r]$ is a subset of $[\Phi]$. The nodal actuator forces are then given by

$$\{F_{act}\} = [k]\left(\{\delta_{cmd}\} - [r]\{\xi\} - [a][r]\{\dot{\xi}\}\right) \tag{34}$$

Finally, the modal acutator force is given by

$$\{\tilde{F}_{act}\} = [r]^T\{F_{act}\} = [r]^T[k]\left(\{\delta_{cmd}\} - [r]\{\xi\} - [a][r]\{\dot{\xi}\}\right) \tag{35}$$

V. Aeroservoelastic State Space Model

The assembled aeroservoelastic state-space model is obtained by combining Eqs. (7), (23), (24), and (35) together to give

$$\left\{ \begin{array}{c} \dot{\xi} \\ \ddot{\xi} \\ \dot{z} \end{array} \right\} = \begin{bmatrix} 0 & I & 0 \\ -\widehat{M}^{-1}\widehat{K} & -\widehat{M}^{-1}\widehat{C} & q_\infty\widehat{M}^{-1}C_A \\ 0 & B_A^1 & A_A \end{bmatrix} \left\{ \begin{array}{c} \xi \\ \dot{\xi} \\ z \end{array} \right\} + \begin{bmatrix} 0 \\ \widehat{M}^{-1}r^T k \\ 0 \end{bmatrix} \{\delta_{cmd}\} \tag{36}$$

and for acceleration output

$$\{y\} = \left[\begin{array}{ccc} -\Phi\widehat{M}^{-1}\widehat{K} & -\Phi\widehat{M}^{-1}\widehat{C} & q_\infty\Phi\widehat{M}^{-1}C_A \end{array}\right]\left\{\begin{array}{c} \xi \\ \dot{\xi} \\ z \end{array}\right\} + \left[\Phi\widehat{M}^{-1}r^T k\right]\{\delta_{cmd}\} \tag{37}$$

Here, $[\widehat{M}]$, $[\widehat{C}]$, $[\widehat{K}]$ are given by

$$\begin{aligned} \left[\widehat{M}\right] &= \left[\widetilde{M}\right] - q_\infty\left[D_A^2\right] && (38) \\ \left[\widehat{C}\right] &= \left[\widetilde{C}\right] - q_\infty\left[D_A^1\right] + \left[r\right]^T\left[k\right]\left[a\right]\left[r\right] && (39) \\ \left[\widehat{K}\right] &= \left[\widetilde{K}\right] - q_\infty\left[D_A^0\right] + \left[r\right]^T\left[k\right]\left[r\right] && (40) \end{aligned}$$

If instead of acceleration, displacement is requested as the output, the set of linear output equations are given by

$$\{y\} = \left[\begin{array}{ccc} \Phi & 0 & 0 \end{array}\right]\left\{\begin{array}{c} \xi \\ \dot{\xi} \\ z \end{array}\right\} \tag{41}$$

Likewise, if velocity is desired as the output, the linear output equations are given by

$$\{y\} = \left[\begin{array}{ccc} 0 & \Phi & 0 \end{array}\right]\left\{\begin{array}{c} \xi \\ \dot{\xi} \\ z \end{array}\right\} \tag{42}$$

In summary form, the aeroservoelastic (ASE) model is given as

$$\{\dot{x}\} = [A_{ase}]\{x\} + [B_{ase}]\{u\} \tag{43}$$

with

$$\{y\} = [C_{ase}]\{x\} + [D_{ase}]\{u\} \tag{44}$$

where $\{x\}$ is given by

$$\{x\} = \left\{\begin{array}{c} \xi \\ \dot{\xi} \\ z \end{array}\right\} \tag{45}$$

and $\{u\}$ is given by

$$\{u\} = \{\delta_{cmd}\} \tag{46}$$

VI. Interpolated Aerodynamic Models

The aerodynamic models are to be interpolated. Three possible choices exist for which domain to interpolate these models in. These are the time, angular frequency, and reduced frequency domains. However, the time and angular frequency domains correspond to one another. Hence, there are really only two independent choices for the interpolation domain. Nevertheless, both choices can be represented as follows for interpolated flight condition F as follows. In the time domain, the aerodynamic model for interpolated flight condition F is

$$\{\dot{z}\} \quad = \quad [A_A]_F\{z\} + \left[\begin{array}{ccc} 0 & B_A^1 & 0 \end{array}\right]_F\left\{\begin{array}{c} \xi \\ \dot{\xi} \\ \ddot{\xi} \end{array}\right\} \tag{47}$$

$$\{\widetilde{F}_{aero}\} = q_F \left([C_A]_F\{z\} + [\ D_A^0 \quad D_A^1 \quad D_A^2\ ]_F \left\{ \begin{array}{c} \xi \\ \dot{\xi} \\ \ddot{\xi} \end{array} \right\} \right) \tag{48}$$

whereas in the reduced frequency domain it is

$$[Q(p_F)]_F = [A^0]_F + p_F[A^1]_F + p_F^2[A^2]_F + \sum_{l=1}^{N_l} \frac{p_F[B^l]_F}{p_F + \beta_F^l} \tag{49}$$

with

$$p_F = ik_F = i\left(\frac{c}{2V_F}\right)\omega_F \tag{50}$$

A. Interpolation in the time domain

At first glance, it is very tempting to interpolate the time-domain state-space models given by Eqs. (23) and (24) directly. That is, one would want to produce the following representation for the interpolated flight condition F as follows:

$$[A_A]_F = \sum_{i=1}^{N} w_i[A_A]_i \tag{51}$$

$$[B_A^1]_F = \sum_{i=1}^{N} w_i[B_A^1]_i = [B_A^1] = \text{constant} \tag{52}$$

$$[C_A]_F = \sum_{i=1}^{N} w_i[C_A]_i \tag{53}$$

$$[D_A^0]_F = \sum_{i=1}^{N} w_i[D_A^0]_i \tag{54}$$

$$[D_A^1]_F = \sum_{i=1}^{N} w_i[D_A^1]_i \tag{55}$$

$$[D_A^2]_F = \sum_{i=1}^{N} w_i[D_A^2]_i \tag{56}$$

where w_i denote the weights with

$$\sum_{i=1}^{N} w_i = 1 \tag{57}$$

This corresponds to the following non-uniform interpolation in the reduced frequency domain:

$$[A^0]_F = \sum_{i=1}^{N} w_i[A^0]_i \tag{58}$$

$$[A^1]_F = \sum_{i=1}^{N} w_i\left(\frac{V_F}{V_i}\right)[A^1]_i \tag{59}$$

$$[A^2]_F = \sum_{i=1}^{N} w_i\left(\frac{V_F}{V_i}\right)^2[A^2]_i \tag{60}$$

$$[B^l]_F = \sum_{i=1}^{N} w_i [B^l]_i \tag{61}$$

$$\beta_F^l = \sum_{i=1}^{N} w_i \left(\frac{V_i}{V_F}\right) \beta_i^l \tag{62}$$

At the heart of interpolating directly in the time domain are the following assumptions:

$$t_i = t_F = t \qquad \omega_i = \omega_F \qquad k_i \neq k_F \tag{63}$$

Although it possible to interpolate directly in the time domain, doing so is not consistent with how the aerodynamic state-space models were originally generated using Eq. (20). That is, the basis of each of the aerodynamic models is the curve-fit that was done in the reduced frequency domain. Hence, interpolating directly in the time domain using Eqs. (51)-(56) is an inconsistent approximation at best.

B. Interpolation in the reduced frequency domain

On the other hand, interpolating the aerodynamic models in the reduced frequency domain before calculating the corresponding time domain state-space model for flight condition F is self-consistent. The interpolation in the reduced frequency domain is accomplished using

$$[A^0]_F = \sum_{i=1}^{N} w_i [A^0]_i \tag{64}$$

$$[A^1]_F = \sum_{i=1}^{N} w_i [A^1]_i \tag{65}$$

$$[A^2]_F = \sum_{i=1}^{N} w_i [A^2]_i \tag{66}$$

$$[B^l]_F = \sum_{i=1}^{N} w_i [B^l]_i \tag{67}$$

$$\beta_F^l = \sum_{i=1}^{N} w_i \beta_i^l \tag{68}$$

This corresponds to the following time domain interpolation:

$$[A_A]_F = \sum_{i=1}^{N} w_i \left(\frac{V_F}{V_i}\right) [A_A]_i \tag{69}$$

$$[B_A^1]_F = \sum_{i=1}^{N} w_i [B_A^1]_i = [B_A^1] = \text{constant} \tag{70}$$

$$[C_A]_F = \sum_{i=1}^{N} w_i [C_A]_i \tag{71}$$

$$[D_A^0]_F = \sum_{i=1}^{N} w_i [D_A^0]_i \tag{72}$$

$$[D_A^1]_F = \sum_{i=1}^{N} w_i \left(\frac{V_i}{V_F}\right) [D_A^1]_i \tag{73}$$

$$[D_A^2]_F \quad = \quad \sum_{i=1}^{N} w_i \left(\frac{V_i}{V_F}\right)^2 [D_A^2]_i \tag{74}$$

That is, it is necessary to do a non-uniform interpolation in the time-domain in order to achieve a uniform interpolation in the reduced frequency domain. Of course, the underlying assumptions for interpolating directly in the reduced frequency domain is that

$$k_i = k_F = k \qquad \omega_i = \left(\frac{V_i}{V_F}\right)\omega_F \qquad t_i = \left(\frac{V_F}{V_i}\right)t_F \tag{75}$$

That is, assuming that the reduced frequencies from different flight conditions have the same physical meaning implies that angular frequencies and time scales for the different flight conditions have different meanings. An equivalent statement is that Eqs. (69)-(74) correspond to what is needed to put each time domain aerodynamic model on the same physical time scale for interpolation. Although not shown here, using Eq. (75) along with Eqs. (21) and (22) written for time scale t_i, the results for Eqs. (69)-(74) can be determined directly by transforming the time scale of each aerodynamic model from t_i to t_F and summing and weighting appropriately.

VII. Interpolated Aeroservoelastic Systems

A. Methodology

The aerodynamic models which are interpolated in the reduced frequency domain are then combined with the structural and actuator models to generate the final aeroservoelastic matrices. In order to be able to assess the flutter stability characteristics for an unanalyzed point, a family of aeroservoelastic models are generated in two steps. In the first step, the aerodynamic matrices $[A_A]_F$, $[B_A^1]_F$, $[C_A]_F$, $[D_A^0]_F$, $[D_A^1]_F$, $[D_A^2]_F$ are calculated using an appropriate interpolation scheme. These matrices correspond to an aerodynamic state-space model for a unit dynamic pressure. In the second step, the actual aeroservoelastic models for a range of dynamic pressures are generated by scaling the aerodynamic modal forces appropriately as given by Eq. (48).

B. Stability evaluation

The aeroservoelastic state-space models have the form given by Eqs. (43) and (44). For such linear time invariant systems, the exact solution for the state vector is given by

$$\{x(t)\} = e^{[A_{ase}]t}\{x(0)\} + \int_0^t e^{[A_{ase}](t-\tau)}[B_{ase}]\{u(\tau)\}\,d\tau \tag{76}$$

Hence, the system characteristics will be determined by the eigenvalues of $[A_{ase}]$. These eigenvalues are represented using the following form:

$$\lambda_i = -\zeta_i\omega_i \pm i\omega_i\sqrt{1-\zeta_i^2} \tag{77}$$

where the angular frequency ω_i is given by

$$\omega_i = |\lambda_i| \tag{78}$$

and the damping ζ_i is given by

$$\zeta_i = -\frac{Re(\lambda_i)}{\omega_i} = -\frac{1}{2}g_i \tag{79}$$

Here, g_i corresponds to the damping that is typically used in aeroelastic and aeroservoelastic analysis.

The aeroservoelastic system is stable if the real part of the eigenvalues are negative in value leading to all unforced initial condition responses decaying to zero as time increases. This corresponds to $\zeta_i > 0$ and $g_i < 0$. Of course, if $\zeta_i < 0$ and $g_i > 0$, the system will have an unforced initial condition response that is unstable and grows unbounded in time. Finally, neutral stability corresponds to $\zeta_i = g_i = 0$.

Even if the base aerodynamic matrices $[A_A]_F$, $[B_A^1]_F$, $[C_A]_F$, $[D_A^0]_F$, $[D_A^1]_F$, $[D_A^2]_F$ are held constant, the various aeroservoelastic matrices that can generated using those matrices with different dynamic pressures (q_∞'s) will have eigenvalues for the various aeroservoelastic modes which vary with the applied dynamic pressure. Hence, for the present developments, the base aerodynamic matrices are held constant and q_∞ is increased from zero to a value large enough to give an unstable aeroservoelastic system. The dynamic pressure for the onset of flutter instability is then found as that for neutral stability.

It should be noted that the present methodology is linear in nature. That is the starting models for the structural dynamics, actuator dynamics, and aerodynamics are all linear. However, it is possible for each of those models to be a linearization about a nonlniear state. Nevertheless, once the linearization is made, it is not possible to pick-up any further nonlinearities. Thus, for the present approach is not possible to tell if the instabilities found would ultimately correspond to pure flutter or a limit cycle oscillation if all the physical nonlinearities were properly taken into account. In all of the numerical examples, the onset of instabilities will be referred to as the onset of flutter.

VIII. Control Law Design

The plant model described above is combined with a linear quadratic Guassian (LQG) controller. An LQG design consists of a linear quadratic regulator (LQR) combined with a Kalman filter (KF) observer. Here, the Kalman filter is designed with loop recovery.

A. Plant State-Space Model

The plant ASE state-space model is given in the standard form for linear time-invariant (LTI) systems with both process and measurement noise as follows:

$$\{\dot{x}\} = [A_{ase}]\{x\} + [B_{ase}]\{u\} + \{W\} \tag{80}$$

$$\{y\} = [C_{ase}]\{x\} + [D_{ase}]\{u\} + \{V\} \tag{81}$$

where the n states are contained in the vector $\{x\}$, the m inputs are contained in the vector $\{u\}$, the l measured outputs are contained in the vector $\{y\}$ and the process and measurement noises are contained in the vectors $\{W\}$ and $\{V\}$, respectively. Here the process and measurement noises are taken to be uncorrelated white noise.

B. LQR Model

The objective function to be minimized for the LQR problem for the LTI system without system or measurement noise is

$$J(t, t_f) = \int_t^{t_f} \left(\{x(\tau)\}^T [Q(\tau)] \{x(\tau)\} + \{u(\tau)\}^T [R(\tau)] \{u(\tau)\} \right) d\tau \tag{82}$$

where $[Q(\tau)]$ and $[R(\tau)]$ are both positive definite. For the present developments, t_f is taken to be ∞ and the $[Q]$ and $[R]$ matrices are taken to be constant and to have the following form:

$$[Q] = q_x[I] \tag{83}$$

$$[R] = q_u[I] \tag{84}$$

Although not as general as possible, the weighting between the error and the control power can be specified by choosing scalar parameters q_x and q_u appropriately.

The minimization is to be obtained with full state feedback

$$\{u\} = -[K_{ase}]\{x\} \tag{85}$$

where $[K_{ase}]$ represents a matrix of optimal gains that minimize J. Here for the purposes of this problem statement, all the states are assumed to be available. Later, these states will be replaced by the estimated states from the estimator. As shown in Refs. 7 and 8, it is a straightforward task to show that the optimal gain is given by

$$[K_{ase}] = [R]^{-1}[B_{ase}]^T[P] \tag{86}$$

where $[P]$ is the solution to the algebraic Riccati equation, given by

$$[A_{ase}]^T[P] + [P][A_{ase}] + [Q] - [P][B_{ase}][R]^{-1}[B_{ase}]^T[P] = [0] \tag{87}$$

As noted previously, the states of the system are to be estimated; thus, the feedback vector is given by:

$$\{u\} = -[K_{ase}]\{\hat{x}\} \tag{88}$$

where $\{\hat{x}\}$ represents the estimated states. Hence, the closed-loop plant model becomes:

$$\begin{aligned} \{\dot{x}\} &= [A_{ase}]\{x\} - [B_{ase}][K_{ase}]\{\hat{x}\} + \{W\} \quad (89) \\ \{y\} &= [C_{ase}]\{x\} - [D_{ase}][K_{ase}]\{\hat{x}\} + \{V\} \quad (90) \end{aligned}$$

C. Kalman Filter/Estimator Design

The Kalman filter design problem is also well known. See for example Ref. 9. Let $E(\cdot)$ represent the expected value, and assume that $\{W\}$ and $\{V\}$ are unbiased, independent white noise, and that the $n + l$ channels are uncorrelated. This gives:

$$\begin{aligned} E(\{W(t_1)\}\{W(t_2)\}^T) &= [M]\delta(t_1 - t_2) \quad (91) \\ E(\{V(t_1)\}\{V(t_2)\}^T) &= [N]\delta(t_1 - t_2) \quad (92) \\ E(\{W(t)\}\{V(t)\}^T) &= [0] \quad (93) \end{aligned}$$

where $[M]$ and $[N]$ are diagonal matrices representing the process noise covariance and the measurement noise covariance, respectively, and δ is the Dirac delta generalized function. Later on, the $[M]$ and $[N]$ matrices will become design parameters used to accomplish loop recovery. Although $[M]$ was used previously to represent the mass matrix, it should be clear from the context in the following equations that $[M]$ here denotes the process noise covariance.

The state estimator has the following state-space model:

$$\begin{aligned} \{\dot{\hat{x}}\} &= [A_{ase}]\{\hat{x}\} + [B_{ase}]\{u\} - [L_{ase}]^T(\{\hat{y}\} - \{y\}) \quad (94) \\ \{\hat{y}\} &= [C_{ase}]\{\hat{x}\} + [D_{ase}]\{u\} \quad (95) \end{aligned}$$

where $[L_{ase}]$ represents the gain of the Kalman filter. Let the estimation error be represented as $\{e\}$ with

$$\{e\} = \{x\} - \{\hat{x}\} \tag{96}$$

This error will evolve according to the following equation:

$$\{\dot{e}\} = \left[[A_{ase}] - [L_{ase}]^T[C_{ase}]\right]\{e\} + \{W\} - [L_{ase}]^T\{V\} \tag{97}$$

The quantity to be minimized is the scalar cost function

$$J = E(\{e\}^T[\hat{W}]\{e\}) \tag{98}$$

where $[\hat{W}]$ is a symmetric positive definite weighting matrix. The symmetric error covariance matrix is given by

$$[P] = E(\{e\}\{e\}^T) \tag{99}$$

It can be shown through straightforward manipulations that the optimal gain $[L_{ase}]$ is given by

$$[L_{ase}] = [N]^{-1}[C_{ase}][P] \tag{100}$$

with $[P]$ satisfying the following algebraic Riccati equation:

$$[A_{ase}][P] + [P][A_{ase}]^T + [M] - [P][C_{ase}]^T[N]^{-1}[C_{ase}][P] = [0] \tag{101}$$

The full-state feedback optimal quadratic designs have attractive robustness properties that may disappear with the introduction of a state estimator.[7] These robustness properties may be recovered for a minimum phase plant model using the loop recovery technique first presented in Ref. 10 where $[M]$ and $[N]$ are relaxed to be design parameters. Specifically in the present developments, the following choices are made:

$$\begin{aligned} [M] &= q_w[B_{ase}][B_{ase}]^T \quad (102) \\ [N] &= q_v[I] \quad (103) \end{aligned}$$

where the scalars q_w and q_v are chosen to give an appropriate weighting between the psuedo-process and measurement noises, respectively.

Applying the estimated state feedback (Eq. (88)) to the estimator state-space equations given by Eqs. (94) and (95) and employing Eqs. (80) and (81) with the noise terms neglected gives the following controller state-space system:

$$\begin{aligned}\{\dot{\hat{x}}\} &= \left([A_{ase}] - [B_{ase}][K_{ase}] - [L_{ase}]^T[C_{ase}] + [L_{ase}]^T[D_{ase}][K_{ase}]\right)\{\hat{x}\} + [L_{ase}]^T\{y\} && (104)\\ \{u\} &= [K_{ase}]\{\hat{x}\} && (105)\end{aligned}$$

Hence the controller state-space matrices are

$$\begin{aligned}[A_c] &= [A_{ase}] - [B_{ase}][K_{ase}] - [L_{ase}]^T[C_{ase}] + [L_{ase}]^T[D_{ase}][K_{ase}] && (106)\\ [B_c] &= [L_{ase}]^T && (107)\\ [C_c] &= [K_{ase}] && (108)\\ [D_c] &= [0] && (109)\end{aligned}$$

Note that $[C_c]$ is equal to positive $[K_{ase}]$, because the controller is to be applied to the plant model as negative feedback.

D. Closed Loop System

The controller state-space model is combined as negative feedback into the plant state-space model. The closed-loop system is governed by the following set of equations:

$$\left\{\begin{array}{c}\dot{x}\\ \dot{\hat{x}}\end{array}\right\} = \left[\begin{array}{cc} A_{ase} & -B_{ase}K_{ase}\\ L_{ase}^T C_{ase} & A_{ase} - B_{ase}K_{ase} - L_{ase}^T C_{ase}\end{array}\right]\left\{\begin{array}{c}x\\ \hat{x}\end{array}\right\} + \left[\begin{array}{c}B_{ase}\\ L_{ase}^T D_{ase}\end{array}\right]\{\Delta_{cmd}\} \qquad (110)$$

and

$$\{y\} = \left[\begin{array}{cc} C_{ase} & -D_{ase}K_{ase}\end{array}\right]\left\{\begin{array}{c}x\\ \hat{x}\end{array}\right\} + [D_{ase}]\{\Delta_{cmd}\} \qquad (111)$$

where $\{\Delta_{cmd}\}$ is the additional command input. Using the definition of the error given by Eq. (96), these can be shown to be

$$\left\{\begin{array}{c}\dot{x}\\ \dot{e}\end{array}\right\} = \left[\begin{array}{cc} A_{ase} - B_{ase}K_{ase} & B_{ase}K_{ase}\\ 0 & A_{ase} - L_{ase}^T C_{ase}\end{array}\right]\left\{\begin{array}{c}x\\ e\end{array}\right\} + \left[\begin{array}{c}B_{ase}\\ B_{ase} - L_{ase}^T D_{ase}\end{array}\right]\{\Delta_{cmd}\} \qquad (112)$$

and

$$\{y\} = \left[\begin{array}{cc} C_{ase} - D_{ase}K_{ase} & D_{ase}K_{ase}\end{array}\right]\left\{\begin{array}{c}x\\ e\end{array}\right\} + [D_{ase}]\{\Delta_{cmd}\} \qquad (113)$$

IX. AGARD 445.6 Wing Example

The example problem selected for this development is the AGARD 445.6 configuration which has served as a standard aeroelastic benchmark problem for a number of decades.[11,12] The wing has a root chord of 1.833 ft, a tip chord of 1.208 ft, a semi-span of 2.5 ft, and an aft sweep angle of 45° at the quarter-chord line. Here the material properties are chosen to match the weakened configuration described in Refs. 11,12. Two different conditions will be used for the wing root. In the first case, the wing root will be taken to be fixed and the aeroelastic stablity is evaluated for which experimental data is available from NASA. In the second case, the wing will be made aeroservoelastic by taking the wing root to be rigid, but able to be rotated about its quarter chord point. In the interest of brevity, no interpolation results will be presented for the fixed root case. Rather, the accuracy of the base aeroservoelastic representation will be assessed for that case. For the rotating root case, both interpolation and closed loop results will be generated.

It is noted here that the underlying structural models for the two cases are slightly different. For the fixed-root aeroelastic model, the underlying modal structural dynamics have been provided directly by NASA. These modal structural dynamics are specified directly in terms of modal frequencies, masses and mode shapes. No structural damping is included. Because a finite element model corresponding to that structural dynamic specification was not made available to the present reserach program, a new finite element model is generated for the rotating rigid root case. The structural mode shapes for this model with the wing root temporarily fixed matched the modal plots available for the aeroelastic AGARD 445.6 configuration. Furthermore, the corresponding modal frequencies agreed fairly well with the previous values provided directly by NASA. However, the new finite element values for the modal frequencies are slightly higher, indicating that the new finite element model is slightly too stiff. Nevertheless, the finite element model is taken to be adequate for demonstration purposes, as creating a better finite element model is not feasible, as the actual wing model tested by NASA was constructed from maghony wood (an orthotropic material) and had holes drilled in it and filled with epoxy in order to lower its flutter speed. Having achieved an acceptable finite element model, the boundary conditions are changed to allow the wing root to rotate as a rigid body about its quarter-chord point.

A. Fixed-root aeroelastic case

In order to compare to the experimental flight conditions, it is convenient to compute a mass ratio, μ, which here is defined as

$$\mu = \frac{\bar{m}}{\rho \bar{V}} \tag{114}$$

where $\bar{m}$ is the mass of the wing, ρ is the free stream fluid density, and $\bar{V}$ is the volume associated with the wing. Here the volume is taken as that of a conical frustrum having a root diameter equal to the wing root chord and and a tip diameter equal to the wing tip chord. Using the measurements of the AGARD wing (root chord of 1.833 ft and tip chord of 1.208 ft) gives $\bar{V} = 4.6034$ cubic ft. The mass of the wing model used in the present calculations is $\bar{m} = 0.1284$ slugs.

After μ is known, it is then possible to calculate the flutter speed index, U, given by

$$U = \frac{V}{b_s \, \omega_\alpha \, \mu^{1/2}} \tag{115}$$

where V is the free stream velocity, b_s is the wing root semi-chord, and ω_α is the natural frequency of the first torsional mode of the wing. Here, ω_α is calculated to be 250.0896 rad/s.

Shown in Fig. 1 are both DLM-based and CFD-based ROM data and the experimental data from Ref. 12 for the flutter speed index. Also shown in Fig. 1 is a single data point computed using the aeroelastic capability of CFL3D-AE. First of all, it is evident that the CFD-based and DLM-based results compare well for subsonic Mach numbers. Furthermore, both sets of computational results agree reasonably well with experimental measurements for the subsonic flight conditions. Although both sets of computational results demonstrate the existence of a transonic dip, neither dip prediction agrees exactly with that coming from the experimental data. Of course, DLM-based aerodynamics are not expected to perform well in the transonic regime due to the presence of shocks in the flow over the wing. Recall, shocks are not captured by a DLM-based solution. Hence, the underprediction of the transonic dip by the DLM approach is not unexpected. The CFD-based results are better than those DLM-based results, because the shocks do appear in the Euler flow solution. However, these inviscid Euler flow solution results overpredict the strength of the shocks, as the boundary layer effects are not captured. This explains the overprediction of the magnitude of the transonic dip. This is not the only problem with the aeroservoelastic models generated using linear GAFs computed from a CFD-based approach. The motion of the shocks that occurs during the modal Guassian pulse excitations used for computing the GAFs does not correspond exactly to what would occur in the oscillations leading to flutter instability. It is felt that this is a small issue.

In order to verify that this is indeed a small issue, an aeroelastic solution is computed directly using CFL3D-AE, the aeroelastic version of CFL3D. The structural modes are splined to the CFD mesh and excited with initial velocities. CFL3D-AE then computes the initial condition response using the structural dynamics modal information along with computing the actual Euler (inviscid) flow solution at each time step. The resulting structural modal motions are then monitored to see if they grew, decayed, or remained constant. Recall that the aeroelastic modes will not correspond exactly to the structural modes, as they involve the combination of the aerodynamics and structural dynamics. That is, a structural mechanics mode may and probably does participate in a number of aeroelastic modes. As should be obvious, flutter onset corresponds to the case when one of the aeroelastic modes becomes neutrally stable (neither growing or decaying) for the chosen dynamic pressure.

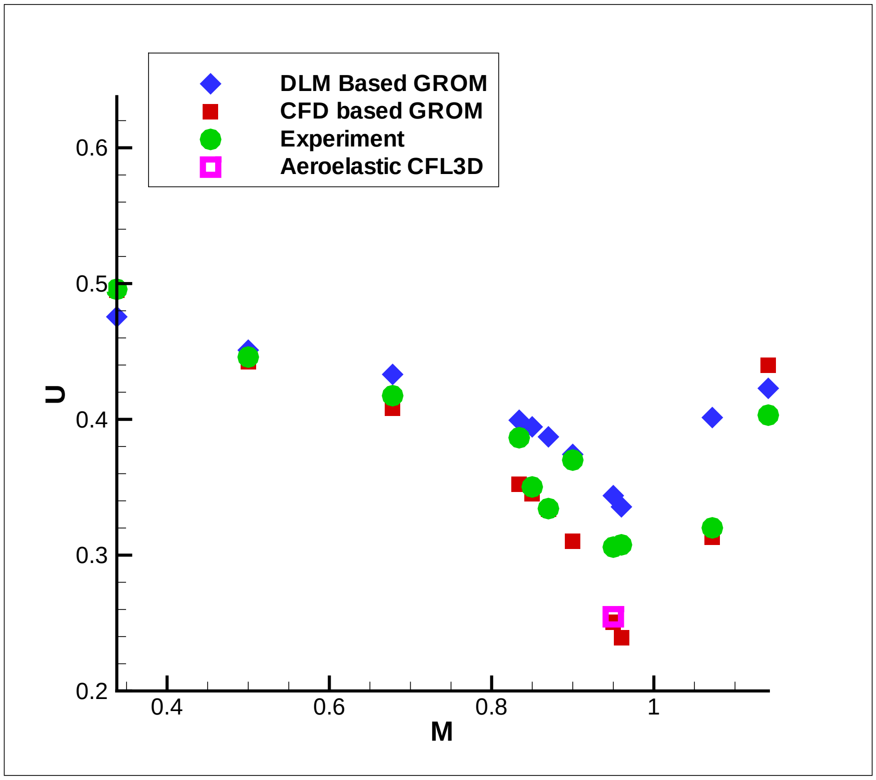

Figure 1. Flutter speed index as a function of Mach number for the aeroelastic fixed-root version of the AGARD 445.6 wing.

In order to see clearly if this is occuring, one must march the aeroelastic solution in the time domain until all of the stable aeroelastic modes along with the initial transients have decayed out. The generalized deflection of the structural modes were plotted and it is taken to be sufficient to check the motion of the first structural mechanics mode over a small number of cycles. Even though this is an approximation designed to limit the computational resources required, it is still computationally very expensive to determine the onset of flutter in this manner (multiple dynamic pressures must be investigated for a single Mach and velocity combination). Hence, only a single point, M =0.95, V = 1060.6 ft/s was investigated. Furthermore, the flutter point was only determined to within the nearest 2.5 psf of dynamic pressure.

Shown in Figs. 2–4 are time histories of the generalized structural modal deflection at several dynamic pressures corresponding to low (30.0 psf), medium (47.5 psf), and high (85.0) values. Here, the modal results for 30.0 psf are clearly stable, while those at 85.0 psf are clearly unstable. Similar types of results were computed at other dynamic pressures in order to compute the flutter onset point. The flutter onset point is determined to be approximately 47.5 psf of dynamic pressure for a Mach number of 0.95 with a velocity of 1060.6 ft/s. Those nearly neutrally stable oscillations are plotted in Fig. 3. Restated as a flutter speed index, the flutter onset point is approximately $U = 0.2546$. This result has also been plotted in Fig. 1 and demonstrates a flutter speed index in the transonic regime comparable to the previous CFD-GAF based state-space model results. Both sets of these CFD-based results overpredict the strength of the transonic dip, as each came from an inviscid Euler flow solution. Hence, the accuracy of the linearized GAF approach has been demonstrated in that most of its overprediction of the transonic dip arises from the use of an Euler flow solution and not from linearization.

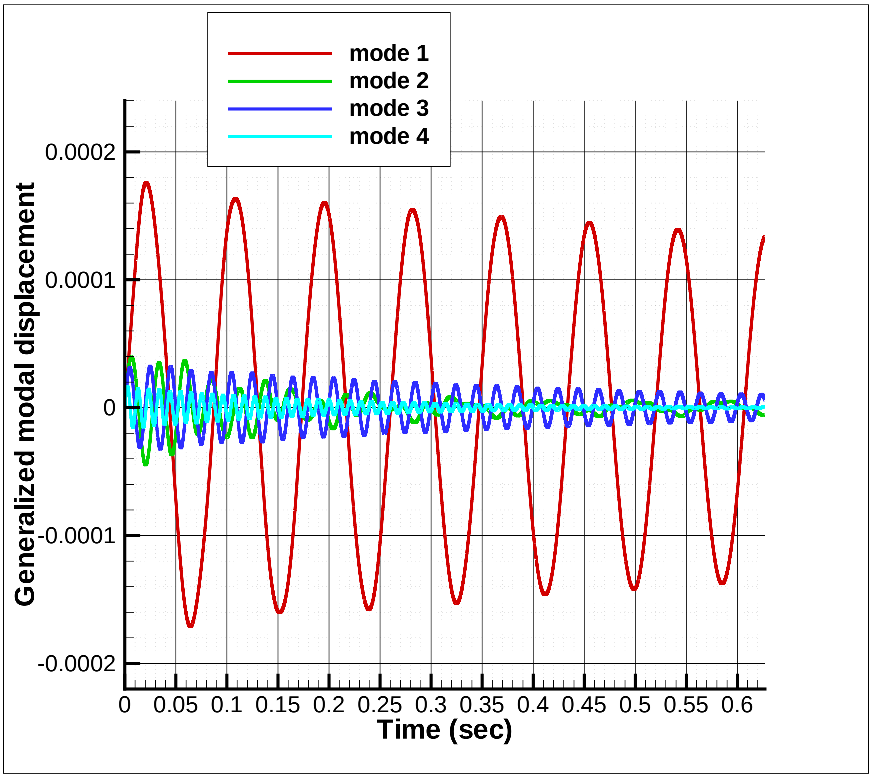

Figure 2. Time history of structural modal motion for M = 0.95, V = 1060.6 ft/s, and q = 30.0 psf (U = 0.2024).

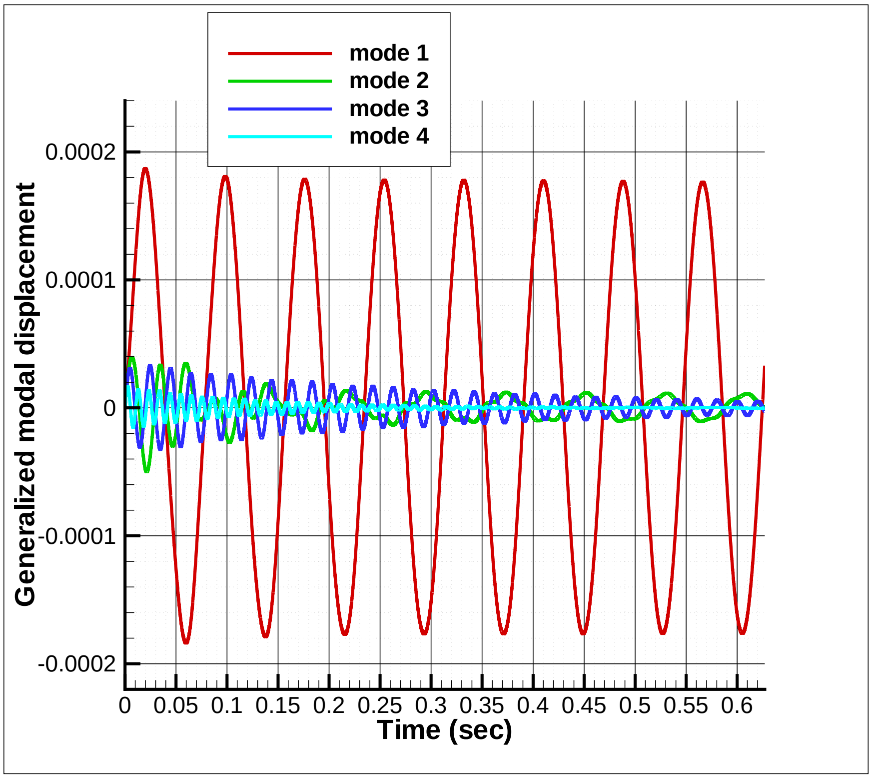

Figure 3. Time history of structural modal motion for M =0.95, V = 1060.6 ft/s, and q =47.5 psf (U = 0.2546).

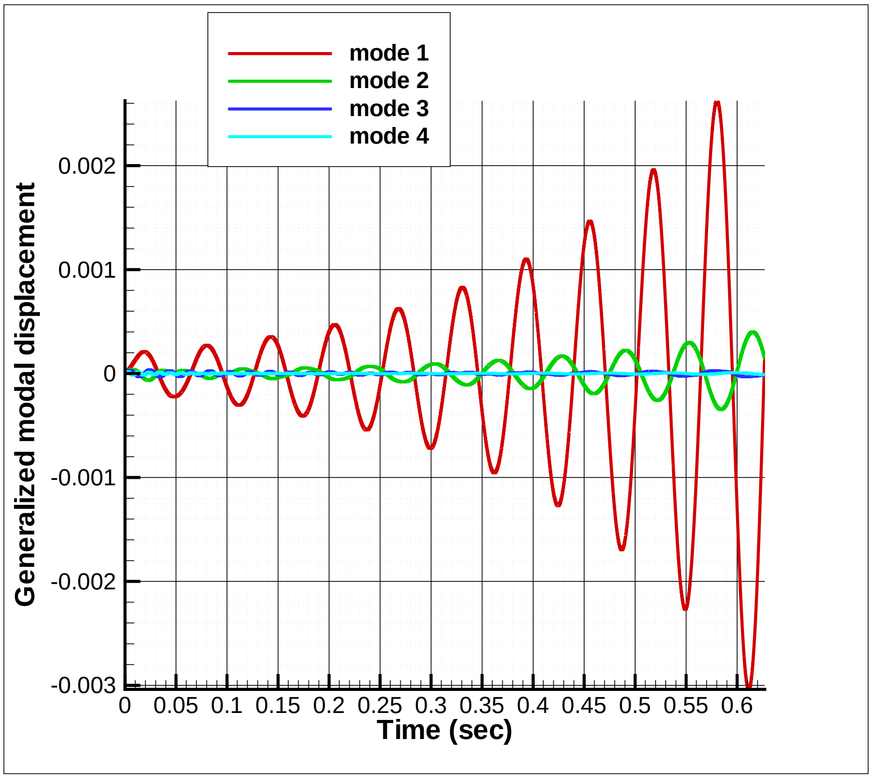

Figure 4. Time history of structural modal motion for M =0.95, V = 1060.6 ft/s, and q = 85.0 psf (U = 0.3406).

B. Rotating rigid root aeroservoelastic case

Having demonstrated the viability of the present linear state-space modeling approach for assessing the flutter of the fixed-root aeroelastic system, the AGARD 445.6 wing is now made aeroservoelastic by allowing the wing root to rotate rigidly about its quarter-chord point. A relatively high stiffness acutator is added to the wing in order to prevent free movement of the wing root. The flutter conditions for this version of the AGARD 445.6 wing are predicted only for the CFD-based linear GAF approach. In all cases, the paths between different flight conditions are taken to correspond to a constant speed of sound of 1081.55 ft/s. That is, the linear relationship between Mach number and free stream velocity is preserved (which would not be the case if the free stream temperature changed over the flight path.)

1. Interpolation and subsequent closed loop model for a subsonic case

First, consider a set of subsonic flight conditions with $M = 0.5$ and V =540.78 ft/s with various dynamic pressures. The velocity is held fixed, while the change in dynamic pressure is taken to result from a change in free stream density. For simplicity, no lag states are used in the RFA representation of the aerodynamic GAFs. Shown in Fig. 5 are plots of the damping and frequency versus dynamic pressure for the first four aeroservoelastic modes computed directly using CFD-based GAFs computed at that Mach and velocity. The flutter point is identified as $q_\infty = 155.9$ psf which corresponds to a flutter speed index of $U = 0.4613$. The flutter point corresponds to the classic case of convergent bending-torsion flutter. Flutter onset is also calculated for $M = 0.338$ with $V = 365.56$ ft/s and $M = 0.678$ with $V = 733.29$ ft/s. The results are presented in Table 1 and Fig. 6.

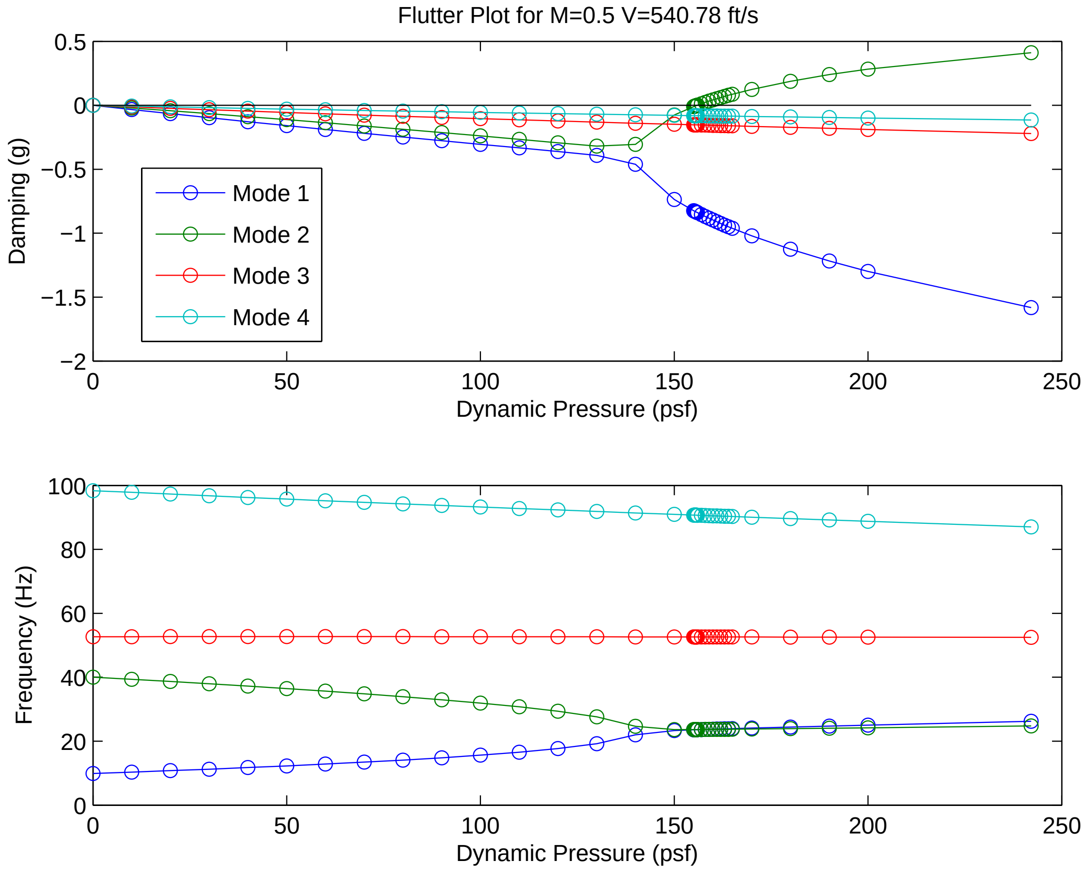

Figure 5. Damping and frequency for the first four aeroservoelastic modes for the rotating root AGARD 445.6 wing at a flight condition of $M = 0.5$ and $V = 540.78$ ft/s.

Table 1. Dynamic pressure and flutter speed index for flutter onset for subsonic flight conditions for the rotating rigid root case. A constant speed of sound of 1081.55 ft/s is used for all flight conditions.

Flight Condition	Mach	Velocity (ft/s)	Flutter Dynamic Pressure (psf)	Flutter Speed Index	Flutter Speed Index Interpolation Error
Direct Evaluation:					
1	0.338	365.56	191.6	0.5114	–
2	0.5	540.78	155.9	0.4613	–
3	0.678	733.29	140.8	0.4384	–
Interpolation:					
2B*	0.5	540.78	154.4	0.4591	-0.48%
2C+	0.5	540.78	–	0.4766	3.32%

*Produced using linear interpolation of the base aerodynamic models from flight conditions 1 & 3
+Produced using linear interpolation of the final flutter results from flight conditions 1 & 3

The interpolated aeroservoelastic models corresponding to $M = 0.5$ and $V = 540.78$ ft/s are generated using a base aerodynamic model which is produced using linear interpolation. That is, the aerodynamic models for the $M = 0.338$ with $V = 365.56$ ft/s and $M = 0.678$ with $V = 733.29$ ft/s cases with $q_\infty = 1$ psf are used to determine that for the $M = 0.5$, $V = 540.78$ ft/s, and $q_\infty = 1$ psf base. The free stream dynamic pressure q_∞ is then varied to find the onset of flutter. The flutter dynamic pressure is found to be $q_\infty = 154.4$ psf which equates to a flutter speed index of $U = 0.4591$. Hence, excellent results have been found for the flutter onset point using a linear interpolation of the base aerodynamic models. Of course, if only the flutter speed index is of interest, it is possible to just curve fit the flutter speed index directly. Doing so in a linear fashion between the $M = 0.338$, $V = 365.56$ ft/s and $M = 0.678$, $V = 733.29$ ft/s results produces a flutter speed index of $U = 0.4766$, an acceptable approximation, but not as accurate as that computed using aeroservoelastic models resulting from a linear interpolation of the base aerodynamic models. Hence, an interpolation of higher order than linear (and requiring additional input points) is needed to produce results of equivalent accuracy. Both sets of interpolation results are also presented in Table 1 and Fig. 6.

A LQG controller is designed for the $M = 0.5$ and $V = 540.78$ ft/s case using the aeroservoelastic models produced using linear interpolation of the base aerodynamic models. The dynamic pressure taken for the design point is taken to be at a free stream dynamic pressure of 231.6 psf which is 150% of the flutter point for the interpolated models. Shown in Fig. 7 are the damping and frequency results as a function of applied dynamic pressure for the closed loop system. Note that the results are separated into the various modes by a simple scheme which sorts the frequencies from lowest to highest at each dynamic pressure separately. Hence, when the frequency lines of the various modes cross, the simple scheme does not properly capture which mode is which. However, the plots in Fig. 7 remain discernible to human inspection. For very small dynamic pressures, the closed loop system is unstable. However, once the free stream dynamic pressure is above 40 psf, no flutter occurs. This result is not entirely surprising, considering the limitations of a single control deflection that rotates the entire wing root. Hence, in order to use such a controller for the rotating rigid root AGARD 445.6, one would need to wait to turn the controller on until sufficient free stream dynamic pressure had been achieved.

2. Interpolation for a transonic case

Now consider the transonic flight conditions with $M = 0.9$, 0.93, 0.95, 0.96, and 0.98 with corresponding velocities for a fixed speed of sound of 1081.55 ft/s. Cubic interpolation will be used to generate the base ($q_\infty = 1$ psf) aerodynamic model for $M = 0.95$ from the other four Mach numbers. In order to assess whether cubic interpolation will be enough and learn more about what type of behavior occurs in the transonic regime, the raw CFD GAF data (without a RFA fit) will first be plotted in the reduced frequency domain for the first five modes. Then, RFA fits will be generated for $M = 0.9$, 0.93, 0.96, and 0.98. These RFA fits will then be interpolated in the reduced frequency domain in a cubic fashion to produce results for $M = 0.95$. Finally, the flutter characteristics of the interpolated models at $M = 0.95$ will be determined.

Shown in Fig. 8 are the in-phase results for the linear CFD GAFs for the $M = 0.9$, 0.93, 0.96, and 0.98, while the corresponding out-of-phase results are shown in Fig. 9. Also shown in these two figures are results for $M = 0.95$ computed directly using CFL3D-AE and from a cubic interpolation of the other CFD

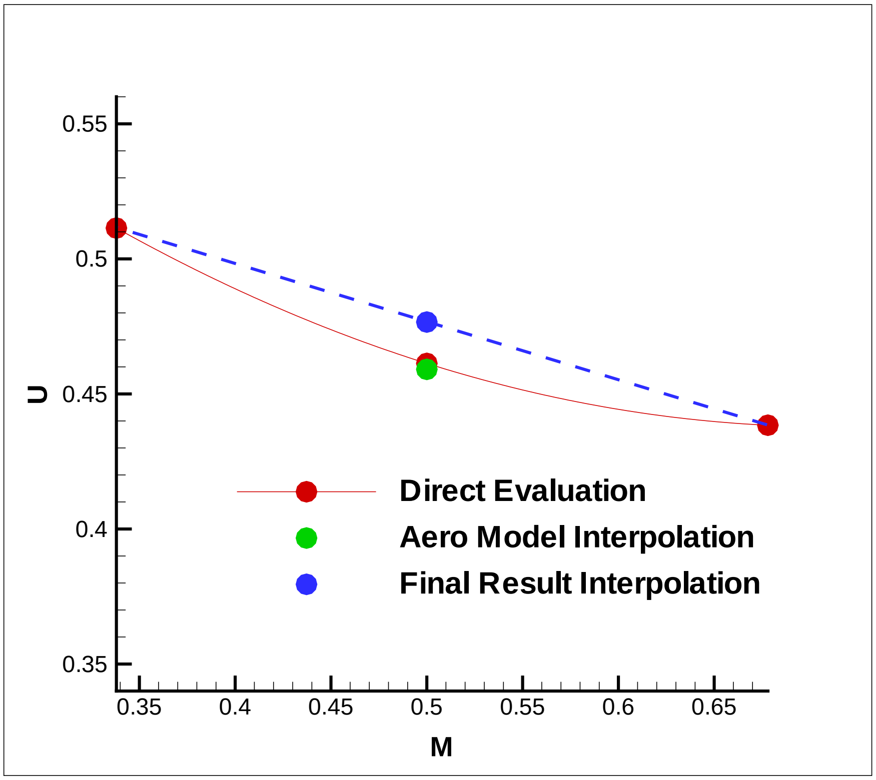

Figure 6. Flutter speed index for AGARD 445.6 with a rotating rigid root at subsonic flight conditions evaluated directly and with interpolation.

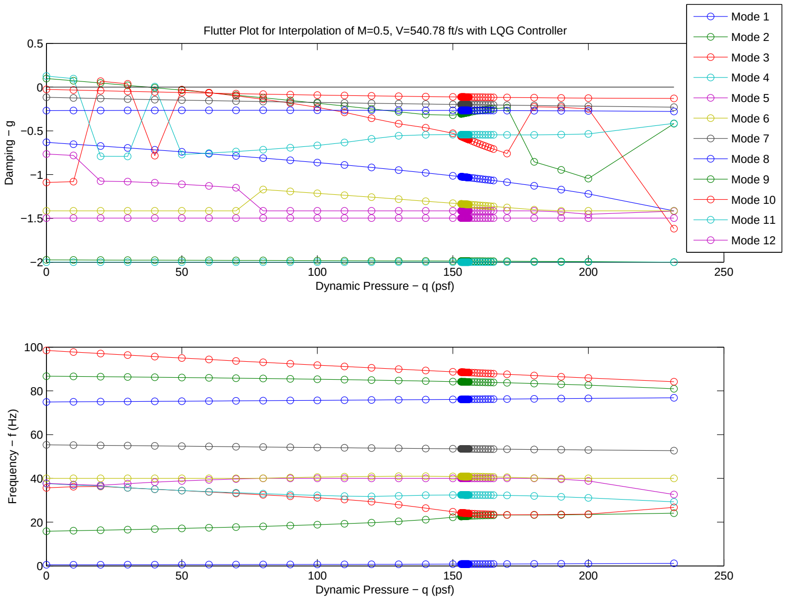

Figure 7. Damping and frequency for the aeroservoelastic modes of the closed loop AGARD 445.6 wing with a rotating rigid root. The other parts of the flight condition consist of a Mach number of 0.5 and a free stream velocity of 540.78 ft/s.

GAFs. Note these results are produced without consideration to RFA fits. However, it should be noted that these show the best results that could possibly be achieved with a series of RFA fits. Note that there is a wide variation in how the GAFs vary with reduced frequencies for the various Mach numbers. However, performing cubic interpolation of the GAF results with a cubic Lagrange polynomial generated for $M = 0.9$, 0.93, 0.96, and 0.98, appears to give good results for the $M = 0.95$ case.

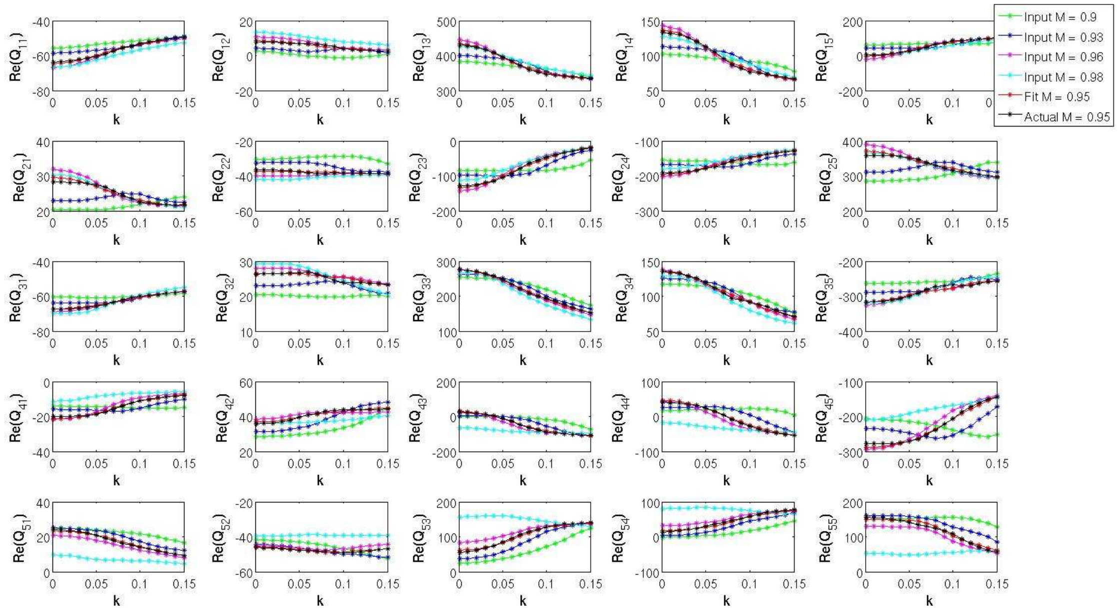

Figure 8. In-phase portions of the GAFs for the transonic flight conditions corresponding to $M = 0.9$, 0.93, 0.96, and 0.98. Results for $M = 0.95$ are shown for actual evaluation at that condition and that coming from a cubic interpolation of the CFD GAF results for input Machs of $M = 0.9$, 0.93, 0.96, and 0.98. Here the speed of sound is taken to be constant at 1081.55 ft/s and the dynamic pressure is 1.0 psf.

Shown in Figs. 10 and 11 are plots of the GAFs as a function of Mach number for reduced frequencies of $k = 0.1$ and $k = 0.15$, respectively. The raw data is plotted, as well as curves for the cubic Lagrange polynomials that pass throu the “input” CFD GAF data at $M = 0.9$, 0.93, 0.96, and 0.98. Also shown are the interpolated results for $M = 0.95$ and the corresponding results for $M = 0.95$ obtained using CFD directly. Note that the interpolations presented in these two figures correspond to interpolation of the raw CFD GAF data and not the yet to be determined RFA fits of that data. Here the CFD data is interpolated for each reduced frequency separately which is analogous to fitting the RFA coefficients as shown in Eqs. (64)-(68). It appears that a cubic fit captures most of the transonic behavior of the GAFs for each individual reduced frequency. Although the cubic interpolation looks different at each reduced frequency, the same weighting factors are to produce the cubic fits for each reduced frequency. It is just that the values being multiplied by the individual weighting factors change for each reduced frequency.

The final results for the RFA fits for the $M = 0.95$, $V = 1027.47$ ft/s, $q = 1.0$ psf case are shown in Fig. 12. The RFA fits produced using CFD directly are plotted as symbols and the cubic interpolation for the RFA fits are shown as lines in Fig. 12.

Having demonstrated the accuracy of a cubic fit to the base transonic aerodynamics (q =1.0 psf) for a constant speed of sound (10811.55 ft/s), results will now be presented for the onset of flutter. Shown in Table 2 and Fig. 13 are results for the transonic Mach numbers under consideration. For $M = 0.95$, both the direct evaluation and interpolation results are shown. The final results created using the interpolated aerodynamics are accurate.

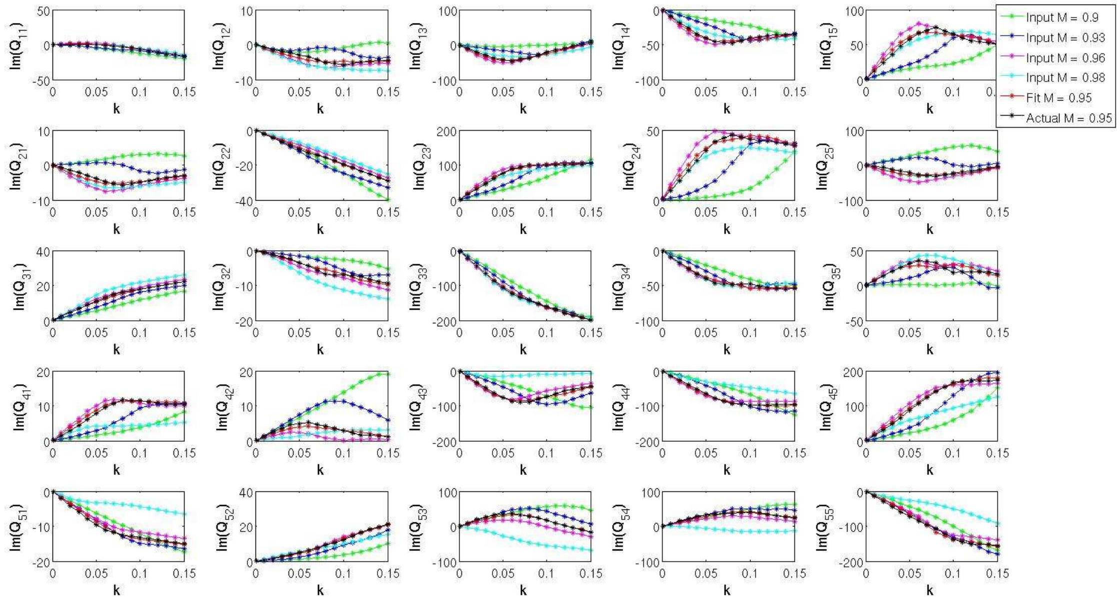

Figure 9. Out-of-phase portions of the GAFs for the transonic flight conditions corresponding to $M = 0.9$, 0.93, 0.96, and 0.98. Results for $M = 0.95$ are shown for actual evaluation at that condition and that coming from a cubic interpolation of the CFD GAF results for input Machs of $M = 0.9$, 0.93, 0.96, and 0.98. Here the speed of sound is taken to be constant at 1081.55 ft/s and the dynamic pressure is 1.0 psf.

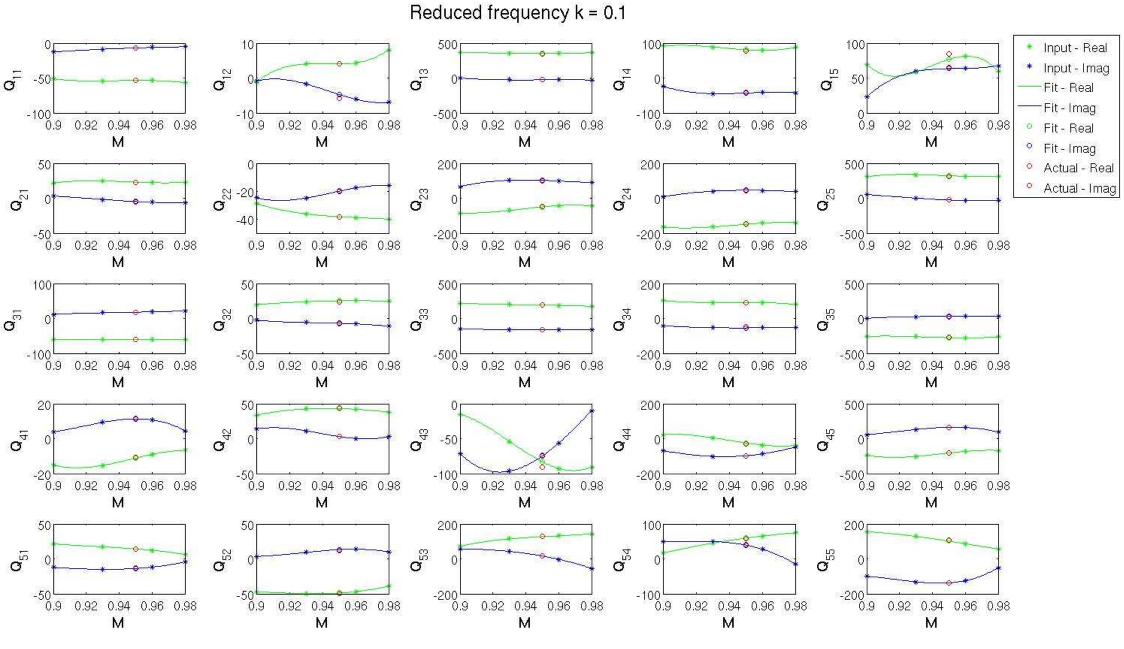

Figure 10. CFD-based GAFs as a function of Mach number for a reduced frequency of $k = 0.1$. Here the speed of sound is taken to be constant at 1081.55 ft/s and the dynamic pressure is 1.0 psf.

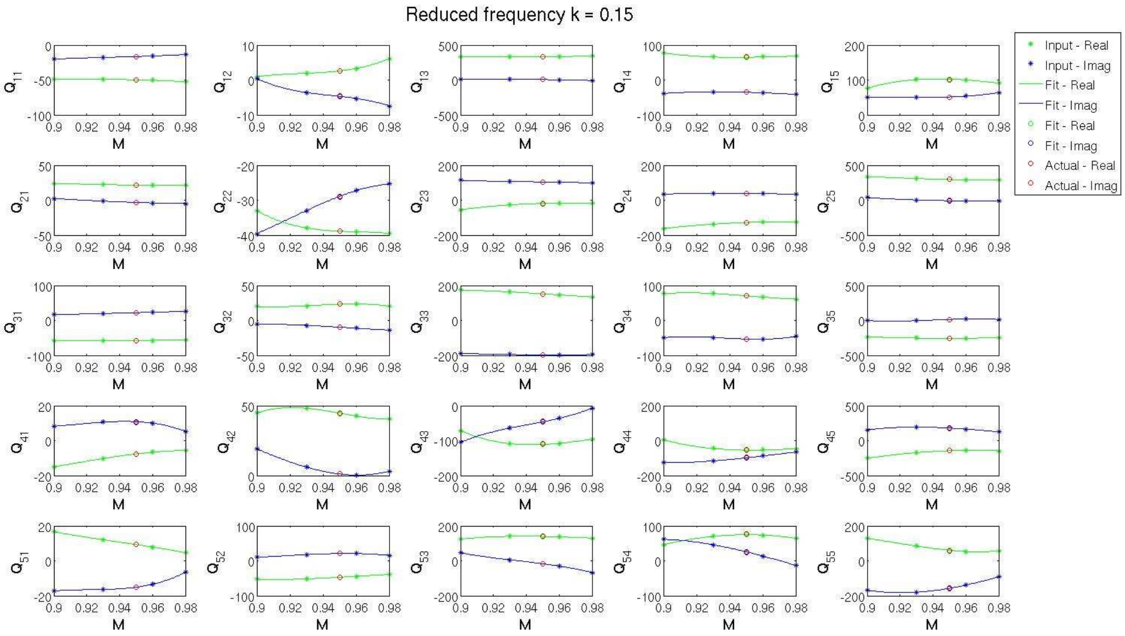

Figure 11. CFD-based GAFs as a function of Mach number for a reduced frequency of $k = 0.15$. Here the speed of sound is taken to be constant at 1081.55 ft/s and the dynamic pressure is 1.0 psf.

Table 2. Dynamic pressure and flutter speed index for flutter onset for transonic flight conditions for the rotating rigid root case.

Flight Condition	Mach	Velocity (ft/s)	Flutter Dynamic Pressure (psf)	Flutter Speed Index
4	0.90	973.40	83.1	0.3368
5	0.93	1005.84	71.6	0.3126
6	0.96	1038.29	59.2	0.2843
7	0.98	1059.92	57.7	0.2806
F	0.95	1027.47	62.4	0.2918
F*	0.95	1027.47	62.7	0.2925

*Produced using cubic interpolation of the base aerodynamic models from flight conditions 4, 5, 6, and 7

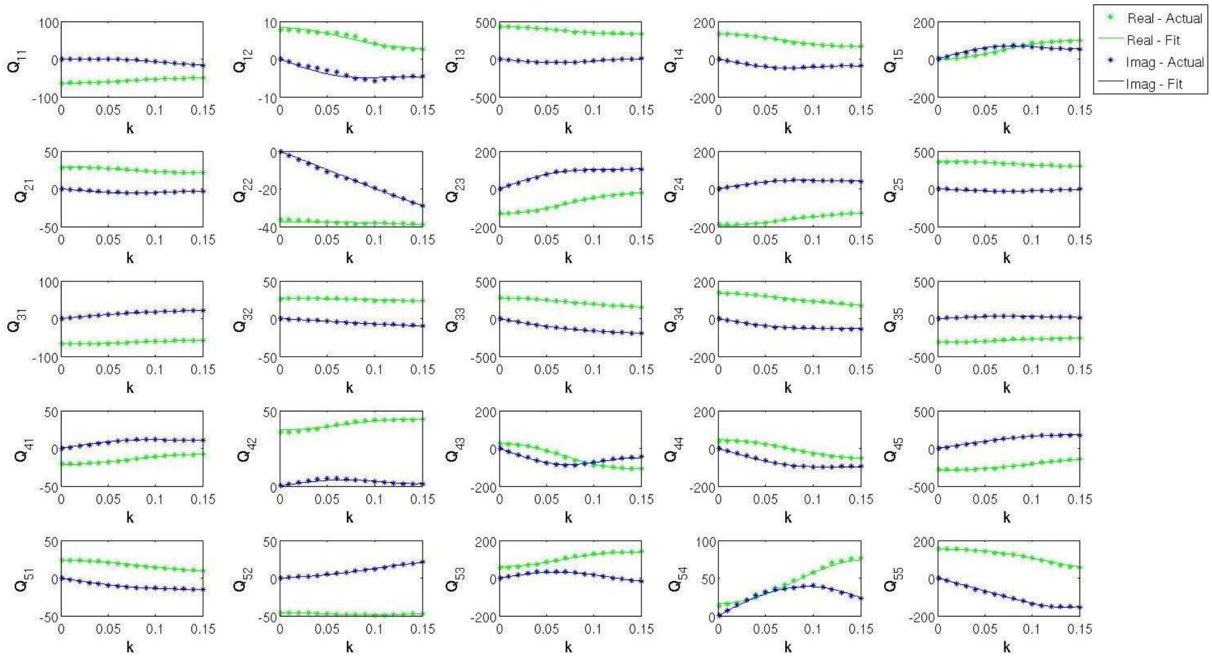

Figure 12. RFA fits for the M =0.95 flight condition produced from direct CFD evaluation and from cubic interpolation of the RFA fits for M =0.9, 0.93, 0.96, and 0.98. Here the speed of sound is taken to be constant at 1081.55 ft/s and the dynamic pressure is 1.0 psf.

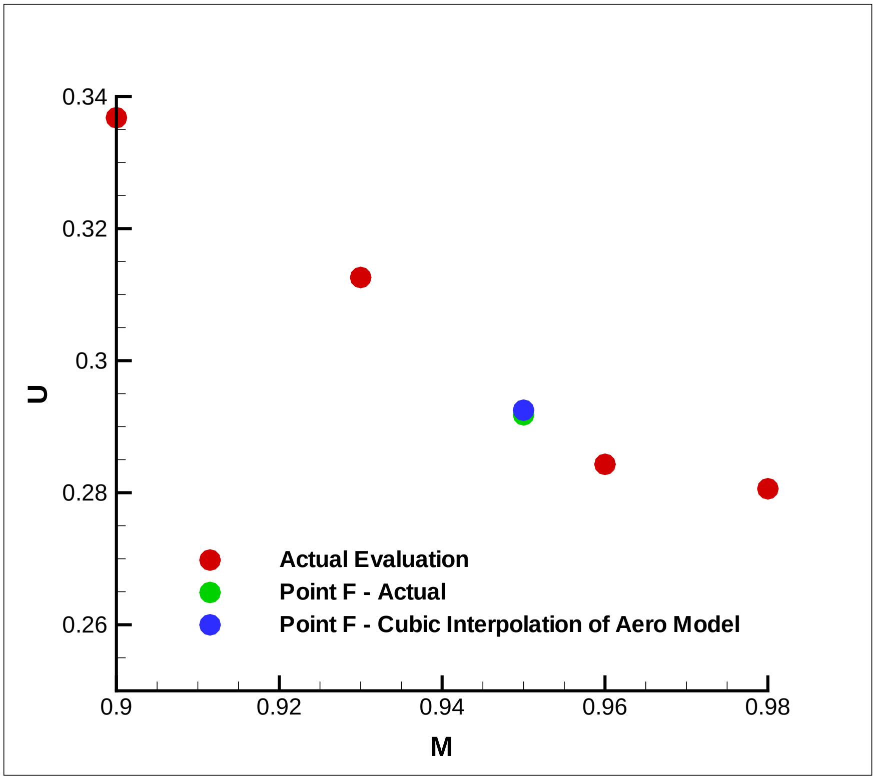

Figure 13. Flutter speed index for AGARD 445.6 with a rotating rigid root at transonic flight conditions evaluated directly and with interpolation. Here the speed of sound is taken as constant at 1081.55 ft/s.

X. Summary

A methodology for creating aeroservoelastic models based on interpolated aerodynamic models has been presented. Using such a methodology it is possible to vary the dynamic pressure while holding the other flight conditions constant to generate a family of aeroservoelastic models. Such a family of models can be used to characterize the flutter boundary of a vehicle, a task which is not possible when the final aeroservoelastic models are interpolated themselves. Furthermore, it is possible to generate a LQG controller to improve the flutter characteristics of the resulting aeroservoelastic models.

It should be noted that several domains exist for where to do the interpolation of the aerodynamic models. Three such choices are the time domain, the angular frequency domain, and the reduced frequency domain. Interpolating in the time domain or the angular frequency domains is equivalent. For the present approach the raw DLM or CFD data for the generalized aerodynamic forces is fit using Roger's RFA in the reduced frequency domain. Hence to be consistent when interpolating the aerodynamic models between different flight conditions, the models must be interpolated in the reduced frequency domain. Although not presented here, interpolating aerodynamic models uniformly in the time domain leads to highly inaccurate results. On the other hand, interpolating such models in the reduced frequency domain has been shown to be accurate using a realistic example. It has been shown in the present developments that interpolating uniformly in the reduced frequency domain corresponds to a non-uniform interpolation in the time domain.

XI. Acknowledgment

Funding for this development has been provided by the Aeroelasticity Branch of NASA Langley Research Center. The NASA technical representative for this research is Walter A. Silva.

References

[1] Bendiksen, O., "Modern Developments in Computational Aeroelasticity," *Proceedings of the Institution of Mechanical Engineers, Part G: Journal of Aerospace Engineering*, Vol. 218, No. 3, 2004, pp. 157–177.

[2] Hammerand, D., Gariffo, J., and Roughen, K., "Improved Computation of Balancing Transformations for Aeroservoelastic Models via Time Scale Conversion," *Journal of Guidance, Control, and Dynamics*, Vol. 34, No. 2, 2011, pp. 475–483.

[3] Giesing, J., Kalman, T., and Rodden, W., "Subsonic Unsteady Aerodynamics for General Configuration," AFFDL-TR-71-5, 1971.

[4] Rodden, W., Harder, R., and Bellinger, E., "Aeroelastic Addition to NASTRAN," NASA CR-3094, 1979.

[5] Bartels, R., Rumsey, C., and Biedron, R., "CFL3D Version 6.4 – General Usage and Aeroelastic Analysis," NASA/TM-2006-214301.

[6] Roger, K., "Airplane Math Modeling Methods for Active Control Design," AGARD-CP-228 Structural Aspects of Active Controls, 1977.

[7] Anderson, B. and Moore, J., *Optimal Control Linear Quadratic Methods*, Dover Publications, Inc., 2007.

[8] Tewari, A., *Modern Control Design with Matlab and Simulink*, John Wiley and Sons, Ltd., 2002.

[9] MIT, *Kalman Filter*, http://ocw.mit.edu/OcwWeb/Mechanical-Engineering/2-154Fall-2004/LectureNotes, 2004.

[10] Doyle, J. and Stein, G., "Robustness with Observers," *IEEE Transactions on Automatic Control*, Vol. AC-24, No. 4, 1979.

[11] Yates, C., "AGARD Standard Aeroelastic Configuration for Dynamic Response I-Wing 445.6," AGARD Report No. 765.

[12] Yates, C., Land, N., and Foughner, J., "Measured and Calculated Subsonic and Transonic Flutter Characteristics of a 45° Sweptback Wing Planform in Air and in Freon-12 in the Langley Transonic Dynamics Tunnel," NASA TN D-1616.